Remote Sensing of Environment 119 (2012) 118–130

Contents lists available at SciVerse ScienceDirect

Remote Sensing of Environment

journal homepage: www.elsevier.com/locate/rse

Global clumping index map derived from the MODIS BRDF product

Liming He [a,*], Jing M. Chen [a,1], Jan Pisek [b], Crystal B. Schaaf [c,d], Alan H. Strahler [c]

[a] Department of Geography and Program in Planning, University of Toronto, 100 St. George St., Room 5047, Toronto, ON, Canada M5S 3G3
[b] Tartu Observatory, Tõravere, 61602 Estonia
[c] Department of Geography and Environment & Center for Remote Sensing, Boston University, 675 Commonwealth Avenue, Boston, MA 02215, USA
[d] Environmental, Earth and Ocean Sciences Department, University of Massachusetts Boston, 100 Morrissey Blvd, Boston, MA 02125, USA

ARTICLE INFO

Article history:
Received 18 January 2011
Received in revised form 12 December 2011
Accepted 13 December 2011
Available online 18 January 2012

Keywords:
Clumping index
MODIS
BRDF
TRAC
Hotspot
NDHD

ABSTRACT

Clumping index (CI), quantifying the level of foliage grouping within distinct canopy structures relative to a random distribution, is a key structural parameter of plant canopies and very useful in ecological and meteorological models. Previously, a Normalized Difference between Hotspot and Darkspot (NDHD) index has been proposed to accurately retrieve the global CI using POLarization and Directionality of the Earth's Reflectances (POLDER) data at ~6 km resolution (Chen et al., 2005). In this study, we show for the first time a global CI map at 500 m resolution derived using the Bidirectional Reflectance Distribution Function (BRDF) product from Moderate Resolution Imaging Spectroradiometer (MODIS), which currently provides the finest pseudo multi-angular data for the global land surface. In computing the NDHD we found that the hotspot calculated from the MODIS BRDF product is underestimated in comparison with POLDER measurements very near the hotspot. Without correcting the bias in MODIS data, the MODIS-derived CI could be overestimated. We have developed an approach to correct the MODIS hotspot magnitude with co-registered POLDER-3 data acquired at about the same time. Field-measured element-CIs in zenith angles of 30–60° by the Tracing Radiation and Architecture of Canopies (TRAC) instrument from 38 sites together with corresponding needle-to-shoot area ratios were used to evaluate the performance of hotspot-corrected NDHD and to tune the parameters to get accurate CI. It is found that the MODIS-derived CI has a dependence on the solar zenith angle, and this dependence in the red band is smaller than that in the near infrared (NIR) band. The highest correlation between field measurements and MODIS-derived CI is achieved when hotspot at nadir is used. The correct estimation of forest species (and therefore the crown shapes) from land cover is very important to the accuracy of MODIS-derived CI. For the red band, the coefficient of determination (R^2) between MODIS-derived CI and field-measured CI is 0.76 for all sites and R^2 is 0.53 for only the needle-leaved forest sites after the hotspot correction, indicating that a strong correlation between MODIS-derived NDHD and CI indeed exists. The MODIS-derived CI is regularly smaller than the field measurement. The red band in the MODIS BRDF product is found to be better than the NIR band for deriving CI for the vegetation covers investigated (mostly dense forests). Therefore a global clumping index map has been produced using the corrected MODIS hot \spot in the red band and optimized parameters. However there were 10 broad-leaved forest sites used in the validation, which are too few for a reliable validation. For the broad-leaved forest area, where the same crown shape (ellipsoid) is used in the algorithm, the global CI spatial pattern is interestingly very similar to the pattern of the land cover distribution, suggesting that the MODIS-derived map has effectively captured the structural differences among cover types.

1. Introduction

Leaves are organized in various canopy structures, and therefore their spatial distributions are often non-random (Chen & Black, 1992). For example, needle-leaved forests are highly organized with structures such as shoots of needles, branches, whorls, tree crowns and tree groups (Chen & Leblanc, 1997). Broad-leaved forests also have distinct ellipsoid or hemi-ellipsoid crown structures which also confine the leaf spatial distribution, making it non-random. Row crops, discontinuous shrubs, and patchy grasses are also examples of non-random canopy structures. These non-random leaf distributions affect the radiation interception and distribution within the canopies and therefore evapotranspiration, energy partitioning, carbon uptake, etc. (Chen et al., in press). The ability to derive the spatial information to quantify these structural effects is therefore highly desirable.

The dispersion or grouping of leaves, relative to a random distribution, is referred to as clumping (Chen & Black, 1992) and has been

* Corresponding author. Tel.: +1 416 978 5070.
E-mail addresses: liming.he@gmail.com (L. He), chenj@geog.utoronto.ca (J.M. Chen).
[1] Tel.: +1 416 978 7085; fax: +1 416 946 3886.

0034-4257/$ – see front matter © 2011 Elsevier Inc. All rights reserved.
doi:10.1016/j.rse.2011.12.008

quantified by a vegetation dispersion parameter Ω at given zenith angle θ (Nilson, 1971):

$$P(\theta) = e^{-G(\theta)L\Omega(\theta)/\cos\theta} \quad (1)$$

where P is the gap proportion, G is the mean projection of unit foliage area in the same direction, and L is the leaf are index (LAI). Ω is also referred to as the clumping index (CI), because its value is generally less than one for vegetation canopies (Chen et al., 2005).

For the purpose of measurements, the total clumping can be separated into two components, the clumping at scales larger and smaller than the shoot, which are measured in the field and in the lab, respectively (Chen, 1996):

$$\Omega(\theta) = \frac{\Omega_e(\theta)}{\gamma_e} \quad (2)$$

where Ω_e is the clumping of foliage elements, which are leaves for broad-leaved species and shoots for needle-leaved species; γ_e is the needle-to-shoot area ratio (Chen & Leblanc, 1997), which accounts for clumping of needles within a shoot, and for broadleaves $\gamma_e = 1$.

$\Omega_e(\theta)$ and therefore $\Omega(\theta)$ generally increases with increasing θ (Kucharik et al., 1997). To avoid the problem of clumping variation with θ, Chen et al. (2005) defined an average CI as:

$$CI = \frac{L_e}{L} \quad (3)$$

where L_e is the effective LAI computed using modified Miller's (1967) theorem (Chen, 1996):

$$L_e = -2\int_0^{\pi/2} \ln[P(\theta)]\cos\theta\,\sin\theta d\theta. \quad (4)$$

Assuming that L and L_e are for a whole canopy, only a single clumping value is produced for the canopy in this way.

CI has been realized as a key structural parameter of plant canopies (Chen et al., 2003; Lacaze et al., 2002). Its significances have been shown in several remote sensing applications (Duthoit et al., 2008; Hill et al., 2011; Pisek et al. 2010a; Ryu et al., 2010b; Simic et al., 2010), and in ecological and meteorological modeling (Baldocchi & Harley, 1995; Chen et al., 2008; Law et al. 2001a; Mo et al., 2008).

Given the global data collection capabilities, remote sensing data have been used to produce CI maps for large areas. Lacaze et al. (2002) found that an angular index based on the hotspot and darkspot (HDS) can be linearly related with CI for three different vegetation types observed by the spaceborne POLDER sensor. The HDS was firstly proposed by Chen et al. (2001) as:

$$HDS = \frac{\rho_{HS} - \rho_{DS}}{\rho_{HS}} \quad (5)$$

where ρ_{HS} is the bidirectional reflectance factor (BRF) at hotspot, and ρ_{DS} is the BRF at darkspot. The hotspot (specifically hotspot correlation effect or hotspot phenomenon) refers to the observed brightening which can occur when viewing a scene from the direction of the illumination, while the darkspot refers to the darkening in the forward scattering direction where the shadow of vegetation is maximally observed. Soon afterward, another angular index (Leblanc et al., 2001), the Normalized Difference between Hotspot and Darkspot (NDHD), was defined as

$$NDHD = (\rho_{HS} - \rho_{DS})/(\rho_{HS} + \rho_{DS}). \quad (6)$$

Chen et al. (2003) found that NDHD is more linearly related to CI than HDS. Canada-wide (Leblanc et al., 2005b) and global (Chen et al., 2005) CI maps were produced based on the NDHD from POLDER measurements at ~6 km resolution. The global CI map was refined by topographic compensation and evaluated against field data (Pisek et al., 2010b). Multi-angular airborne or spaceborne remote sensing data at high resolutions are also found to be useful in mapping CI but confined by the spatial extent (Simic & Chen, 2008; Simic et al., 2010).

The hotspot and darkspot BRFs, and thus the NDHD at various solar zenith angles (θ_s, in radians), can also be reconstructed from the Bidirectional Reflectance Distribution Function (BRDF) parameter product (Schaaf et al., 2002; Schaaf et al., 2011) for the Moderate Resolution Imaging Spectroradiometer (MODIS). Efforts have been made to test if CI can be derived at 500 m using the pseudo multi-angular imagery as this is currently the finest resolution available for the globe on a daily basis (Su & Song, 2008). Recently, high correlation ($R^2 = 0.75$) and low mean absolute error (0.058) between MODIS-derived CIs in the red band and field-measured CIs at 63 sites were reported in the initial exploratory study by Pisek et al. (2011a). The MODIS-derived CI was found to have different sensitivity to savanna woody cover for red and near infrared (NIR) bands (Hill et al., 2011).

In this study, we continue to explore the capability of MODIS BRDF product to derive a global CI using the algorithm developed by Chen et al. (2005) and resolve several issues. The hotspot BRF reproduced from the MODIS BRDF product is consistently smaller than that in the POLDER product (Chen et al., 2003; Maignan et al., 2004; Wang et al., 2010). Without correcting the hotspot bias in the MODIS product, the MODIS-derived CI could be overestimated. We propose a procedure to estimate the POLDER-3 hotspot BRF and use this as a basis for correcting the MODIS hotspot BRF. A compilation of $\Omega_e(\theta)$ measured by Tracing Radiation and Architecture of Canopies (TRAC) instrument and γ_e (Pisek et al., 2011a) is firstly quality-checked for eligibility and then used to select optimized parameters (θ_s, darkspot searching method, and band) for the large dataset processing. A global CI map for year 2006 is produced using optimized parameters. The various factors that may influence the accuracy of this map are discussed.

2. Data

2.1. Field-measured clumping index for validation

TRAC measures Ω_e for a whole canopy at a given θ_s (Chen & Cihlar, 1995a). Pisek et al. (2011a) compiled a $\Omega_e(\theta)$ and γ_e database including 63 sites from a review of the literature. $\Omega_e(\theta)$ divided γ_e gives $\Omega(\theta)$ according to Eq. (2). In this study, we used the coefficient of determination (R^2) between MODIS-derived CI and field-measured $\Omega(\theta)$ to indicate their relationship. We are aware of the limitation by comparing directional $\Omega(\theta)$ to the view-angle-independent CI and will discuss the uncertainty in Section 5.6.

The $\Omega_e(\theta)$ from field measurements with the TRAC represents the average canopy clumping along transects of tens to few hundred meters (Chen & Cihlar, 1995a). This can pose a large problem when the $\Omega(\theta)$ is used to validate CI from remotely sensed data in medium/low resolution, such as MODIS (Pisek et al., 2011a) and POLDER (Pisek et al., 2010b), as the clumping effects measured by TRAC may not match the clumping effect in low resolution pixels. Ideally, a validation of a coarse resolution product, such as our CI product at the MODIS resolution of 500 m, should be made based on a high-resolution map that is compatible with the ground plot size (Chen et al., 2002; Morisette et al., 2002). However, such high-resolution multi-angle data are rarely available for ground sites with CI measurements anywhere over the globe. Therefore for the purpose of validation, we have carefully checked satellite images for each of the 63 sites for their spatial uniformity through the Google Maps®. We excluded 25 sites because the MODIS pixels corresponding to these forest sites are found to be too heterogeneous to match the TRAC transect or some sites are too sparse (<25% canopy cover) in

vegetation cover to invert accurate CI (Chen et al., 2005). There are also some sites with homogeneous forest but occupying only part of the MODIS pixel, and a surrogate pixel with similar and complete forest cover is found nearby. The remaining 38 sites in Table 1 are used to evaluate the MODIS-derived CI. The 38 sites represent uniform covers after the site-by-site visual checking so mismatch in scale is minimized in the evaluation.

2.2. POLDER-3 BRDF database

The space-borne POLDER instrument can sample the surface BRDF of the Earth for view zenith angles (θ_v, in radians) up to 60–70°, and for the full azimuth angle range, at a spatial resolution of about 6 km (Hautecoeur & Leroy, 1998). POLDER-3/PARASOL data acquired from November 2005 to October 2006 have been used to build four BRDF databases in Laboratoire des Sciences du Climat et l'Environnement (Bréon et al., 2007). Their objective is to collect directional information on homogeneous pixels representing the main continental ecosystems. The data are pre-processed to obtain the geocoded, calibrated, cloud screened and atmospherically-corrected land surface BRF for each orbit. A monthly database containing 22,012 BRDFs in 22 land cover classes (GLC, 2003) is used in this study. Each BRDF file in the database includes BRFs from a few to more than 20 orbits for each of the six bands. Each orbit provides up to 16 different directional measurements for a pixel. BRFs measured at bands 670 nm and 865 nm are used to correct the hotspot magnitude reconstructed from the MODIS BRDF product.

2.3. MODIS data

The MODIS BRDF Model Parameters product (MCD43A1, version 5) was produced every eight days by using all high quality observations acquired by both Terra and Aqua over a 16 day period (Schaaf et al., 2002). The product is released in a global 500 m SIN Grid. MCD43A1 data from October 2005 to December 2006 were downloaded from https://lpdaac.usgs.gov/. Subsets of MODIS data covering the validation

Table 1
Characteristics of the compiled 38 validation sites (Pisek, Chen & Nilson, 2011) and the location of MODIS pixel for each site. (LC is for GLC2000 "land cover"; CI is for clumping index derived from MODIS; $\Omega(\theta)$ and $\Omega_e(\theta)$ denote clumping index and element clumping index at a zenith angle θ; the range of θ is in 30°–60°. Υ_e is the needle-to-shoot area ratio; h and v indicate horizontal and vertical MODIS tile numbers in the MODIS BRDF product, and line and column indicate location of MODIS pixel in a tile); surrogate pixels are marked with "*"; the average $\Omega(\theta)$ for sites 11, 31, and 38, respectively, are used to compare with corresponding CIs from MODIS.

ID	Latitude	Longitude	LC	CI	$\Omega(\theta)$	$\Omega_e(\theta)$	Υ_e	h	v	Line	Column	Reference
1	18.8000	98.9000	1	0.63	0.79	0.79	1	27	7	287	869	Nasahara (unpublished data)
*2	−3.4803	38.3439	4	0.53	0.68	0.85	1.25	21	9	834	1984	Gonsamo and Pellikka (2008)
3	−3.3603	38.3417	1	0.69	0.86	0.86	1	21	9	805	1985	Gonsamo and Pellikka (2008)
*4	58.2805	27.3309	2	0.67	0.75	0.75	1	19	3	412	1049	Pisek (unpublished data)
5	56.9500	91.5500	2	0.67	0.84	0.84	1	22	3	731	2382	Leblanc, Chen, Fernandes, Deering and Conley (2005)
6	53.6270	−106.1940	2	0.66	0.74	0.74	1	11	3	1529	1684	Chen et al. (1997)
7	55.5320	−98.4050	2	0.65	0.79	0.79	1	12	3	1071	1033	Chen et al. (1997)
*8	45.3892	−75.1886	2	0.67	0.93	0.93	1	12	4	1106	1725	Leblanc and Chen (2001)
9	45.3803	−75.1967	2	0.62	0.92	0.92	1	12	4	1108	1723	Leblanc and Chen (2001)
10	−43.2000	170.3000	6	0.51	0.62	0.87	1.4	30	13	767	993	Walcroft et al. (2005)
*11	49.5000	18.5400			0.58	0.89	1.53					Homolova (unpublished data)
					0.47	0.67	1.42					
			4	0.50	0.53			19	4	121	488	
*12	58.2953	27.2561	4	0.54	0.59	0.84	1.42	19	3	408	1036	Pisek (unpublished data)
*13	57.2500	91.6000	4	0.50	0.56	0.86	1.53	22	3	660	2293	Leblanc, Chen, Fernandes, Deering and Conley (2005)
*14	57.2333	91.5833	4	0.52	0.56	0.85	1.53	22	3	663	2296	Leblanc, Chen, Fernandes, Deering and Conley (2005)
15	31.3500	35.0333	4	0.62	0.69	0.84	1.21	20	5	2075	2379	Sprintsin et al. (2007)
16	34.9020	−79.4860	4	0.56	0.74	0.9	1.21	11	5	1223	1154	Iiames et al. (2008)
*17	36.3830	−77.0010	4	0.58	0.78	0.94	1.21	11	5	868	1921	Iiames et al. (2004)
*18	45.2100	−68.7400	4	0.50	0.61	0.98	1.6	13	4	1149	375	Richardson (unpublished data)
*19	45.2000	−68.7400	4	0.52	0.55	0.88	1.6	13	4	1150	374	Richardson (unpublished data)
20	44.5000	−121.6167	4	0.50	*0.65*	0.81	1.25	9	4	1319	781	Law, Van Tuyl, Cescatti and Baldocchi (2001)
21	53.9160	−104.6920	4	0.53	0.6	0.85	1.42	11	3	1459	2000	Chen et al. (2006)
22	53.8750	−104.0450	4	0.55	0.65	0.93	1.44	11	3	1469	2077	Chen et al. (2006)
23	53.9870	−105.1170	4	0.52	0.66	0.9	1.36	11	3	1442	1966	Chen et al. (2006)
*24	49.6920	−74.3420	4	0.48	0.59	0.92	1.57	13	4	73	456	Chen et al. (2006)
25	46.4720	−67.1000	4	0.55	0.56	0.96	1.71	13	4	846	908	Chen et al. (2006)
*26	49.9050	−125.3660	4	0.45	0.49	0.81	1.66	9	4	24	2217	Chen et al. (2006)
27	46.4740	−67.0980	4	0.51	0.56	0.96	1.71	13	4	845	909	Chen et al. (2006)
*28	46.4770	−67.0770	4	0.51	0.55	0.94	1.71	13	4	844	913	Chen et al. (2006)
*29	49.2500	−82.0500	4	0.45	0.51	0.88	1.71	12	4	179	1546	Leblanc, Chen, Fernandes, Deering and Conley (2005)
*30	47.1600	−81.7500	4	0.53	0.61	0.82	1.35	12	4	679	1061	Pisek et al. (2010c)
*31	46.0000	−77.4500			0.44	0.91	2.08					Chen and Cihlar (1995b)
					0.68	0.88	1.3					
			4	0.50	0.56			12	4	960	1487	
32	55.9280	−98.6240	4	0.47	0.58	0.82	1.42	12	3	976	1138	Chen and Cihlar (1995b)
33	55.9050	−98.2880	4	0.54	0.66	0.95	1.45	12	3	982	1176	Chen et al. (1997)
34	53.8770	−104.6470	4	0.51	0.53	0.72	1.37	11	3	1469	1993	Chen et al. (1997)
35	55.8800	−98.4840	4	0.46	0.49	0.71	1.45	12	3	988	1141	Chen et al. (1997)
36	53.9870	−105.1220	4	0.50	0.48	0.7	1.45	11	3	1442	1965	Chen et al. (1997)
37	38.4310	−120.9660	2	0.73	0.82	0.82	1	8	5	376	1257	Sonnentag et al. (2007)
38	45.4000	−75.5000	5		0.64	0.87	1.36					Sonnentag et al. (2007)
					0.61	0.87	1.42					
				0.56	0.63			12	4	1103	1676	

sites and observed in the same year as the TRAC measurements were selected. Model parameters (f_{iso}, f_{vol}, and f_{geo}) for MODIS band 1 (red, 620–670 nm) and band 2 (NIR, 841–876 nm) are used in this study. The corresponding data quality product (MCD43A2) in the same resolution was also downloaded from the same ftp site and used in this study: layer BRDF_Albedo_Band_Quality is used to identify the best quality data for the red and NIR bands; layer Snow_BRDF_Albedo is used to choose snow free pixels; the land/water mask comes from the layer BRDF_Albedo_Ancillary.

2.4. The GLC2000 land cover map

The GLC2000 land cover (GLC, 2003) is used to determine the canopy crown shapes, which are required by the algorithm of Chen et al. (2005). Its land cover classification system is described in Table 2.

2.5. Vegetation continuous field map

The percent tree cover layer in MODIS Vegetation Continuous Fields (VCF) product (Collection 4, version 3) was used to examine its relationship with MODIS-derived CI (Hansen et al., 2002; Hansen et al., 2003; Hansen et al., 2007). The valid values of this layer range from 0 to 80% representing the percentage of tree cover at 500 m MODIS pixels.

3. Method

3.1. Background and issues to overcome with use of the MODIS BRDF product

The MODIS BRDF model parameters are inverted from a kernel-driven, linear BRDF model which relies on the weighted sum of an isotropic kernel and two functions (or kernels) of viewing and illumination geometry to determine BRF, (Roujean et al., 1992; Schaaf et al., 2002; Wanner et al., 1995).

$$BRF(\theta_s,\theta_v,\phi,\Lambda) = f_{iso}(\Lambda) + f_{vol}(\Lambda)K_{vol}(\theta_s,\theta_v,\phi) + f_{geo}(\Lambda)K_{geo}(\theta_s,\theta_v,\phi) \quad (7)$$

Table 2
Average statistics for clumping index (CI) values for 2006 based on GLC2000 land cover.

No.	Land cover classes	Mean CI	Std. CI
1	Tree cover, broad-leaved, evergreen	0.66	0.05
2	Tree cover, broad-leaved, deciduous, closed	0.70	0.04
3	Tree cover, broad-leaved, deciduous, open	0.72	0.03
4	Tree cover, needle-leaved, evergreen	0.53	0.04
5	Tree cover, needle-leaved, deciduous	0.57	0.03
6	Tree cover, mixed leaf type	0.69	0.04
7	Tree cover, regularly flooded, fresh water	0.67	0.05
8	Tree cover, regularly flooded, saline water	0.71	0.06
9	Mosaic: tree cover/other natural vegetation	0.71	0.04
10	Tree cover, burnt	0.70	0.04
11	Shrub cover, closed-open, evergreen	0.71	0.05
12	Shrub cover, closed-open, deciduous	0.74	0.04
13	Herbaceous cover, closed-open	0.75	0.05
14	Sparse herbaceous or sparse shrub cover	0.76	0.05
15	Regularly flooded shrub and/or herbaceous cover	0.73	0.04
16	Cultivated and managed areas	0.75	0.04
17	Mosaic: cropland/tree cover/other natural vegetation	0.70	0.04
18	Mosaic: cropland/shrub and/or grass cover	0.75	0.04
19	Bare areas	0.84	0.06
20	Water bodies		
21	Snow and ice		
22	Artificial surfaces and associated areas		
23	No data		

where ϕ is the relative azimuth angle in radian; Λ is the band; the first term (f_{iso}) on the right hand side of Eq. (7) denotes Lambertian reflectance, K_{vol} denotes volume-scattering kernel, K_{geo} denotes geometric–optical kernel; f_{iso}, f_{vol}, and f_{geo} are the kernel coefficients. In the MODIS operational BRDF algorithm, the RossThickLiSparse-Reciprocal kernel combination (referred to as the RTLSR model), which is composed of a Ross-Thick volume-scattering kernel, and a LiSparse-R geometric–optical kernel, is used in processing the global data (Wanner et al., 1995).

The Ross-Thick kernel (with its assumption of a dense leaf canopy) is written as (Roujean et al., 1992):

$$K_{vol}(\theta_s,\theta_v,\phi) = \frac{4}{3\pi}\frac{1}{\cos\theta_s+\cos\theta_v}\cdot\left[\left(\frac{\pi}{2}-\xi\right)\cos\xi+\sin\xi\right]-\frac{1}{3} \quad (8)$$

where ξ is the angle between the observer and the sun relative to the target, defined as

$$\cos\xi = \cos\theta_s\cos\theta_v + \sin\theta_s\sin\theta_v\cos\phi. \quad (9)$$

The geometric scattering Li-sparse kernel is written as (Lucht et al., 2000):

$$K_{geo}(\theta_s,\theta_v,\phi) = k_{LSR} = O(\theta_s,\theta_v,\phi) - \sec\theta_s' - \sec\theta_v' + \frac{1}{2}\left(1+\cos\xi'\right)\sec\theta_v' \quad (10)$$

where,

$$O = \frac{1}{\pi}(t-\sin t\cos t)\left(\sec\theta_s' + \sec\theta_v'\right), \quad (11)$$

$$\cos t = \frac{h}{b}\frac{\sqrt{D^2+(\tan\theta_s'\theta_v'\sin\phi)^2}}{\sec\theta_s'+\theta_v'} \quad (12)$$

$$D = \sqrt{\tan^2\theta_s' + \tan^2\theta_v' - 2\tan\theta_s'\tan\theta_v'\cos\phi} \quad (13)$$

$$\cos\xi' = \cos\theta_s'\cos\theta_v' + \sin\theta_s'\sin\theta_v'\cos\phi \quad (14)$$

$$\theta_s' = \tan^{-1}\left(\frac{b}{r}\tan\theta_s\right), \theta_v' = \tan^{-1}\left(\frac{b}{r}\tan\theta_v\right). \quad (15)$$

For MODIS operational data processing, h/b is set to 2 and b/r is set to 1.

Given a set of BRF observations [$BRF(\Lambda)$] ($1\times n$ matrix) at different angles, the kernel coefficients $F(\Lambda)=[f_{iso}, f_{vol}, f_{geo}]$ in Eq. (7) can be determined by minimizing the root mean square errors (RMSE) between the n measurements [$BRF(\Lambda)$]and the model values (Maignan et al., 2004):

$$F(\Lambda) = \left(K^TK\right)^{-1}K^T[BRF(\Lambda)] \quad (16)$$

where K is a $3*n$ matrix, representing for each of the 3 kernels the column vector of the kernel values for each of the N observation geometries. Furthermore, the weights of determination are computed to establish whether the observations available sufficiently sample the surface reflectance anisotropy. Though the "Λ" is implicit in the following text and equations, we process the data for red and NIR bands, respectively.

Given three high quality kernel coefficients for a pixel from the MODIS BRDF product, the darkspot (if it exists, see the following issue one) and hotspot can be reproduced at any θ_s, and the NDHD is calculated. The relationship between NDHD and CI is found to be dependent on the θ_s:

$$CI(\theta_s) = A(\theta_s)\cdot NDHD + B(\theta_s) \quad (17)$$

where A and B are coefficients determined by the linear regression and tabulated for different θ_s, crown shapes, and bands by model simulations (Chen et al., 2005).

Given the features of the RTLSR model and algorithm of Chen et al. (2005), CI can be calculated from any NDHD for the red and NIR bands at corresponding θ_s and its value should be consistent; however, some issues need to be overcome before using the MODIS BRDF product for accurate global mapping of CI. The purpose of this study is to produce a global CI map with the three issues minimized below.

3.1.1. Issue one: the hotspot BRF in the MODIS BRDF product is consistently smaller than that in the POLDER product, and the darkspot does not always exist in the RTLSR model

The MODIS viewing geometry rarely approaches near-principal plane. Furthermore, the Ross-Thick kernel does not account for the correlation of illumination and observation probability within the same canopy gap, which causes the hotspot (Chen & Cihlar, 1997; Hapke et al., 1996; Roujean et al., 1992), and no explicit hotspot is modeled; its minimum BRF (darkspot) is always on the principal plane on the forward-scattering side (Ross, 1981; Roujean et al., 1992). For the LiSparse-R kernel, a weak hotspot appears in the solar direction, but a darkspot is often not easily located because the BRF in the forward-scattering direction may decrease monotonically with increasing θ_v within the satellite θ_v (Wanner et al., 1995). By introducing the three parameters in the MODIS BRDF product to the RTLSR model, it is possible that the resulting BRDF curves on the principal plane can have no darkspot when the geometric–optical kernel dominates or can have a darkspot but also have BRFs which are larger than the hotspot when volume-scattering dominates, e.g., Fig. 1 in Chen et al. (2003) and Fig. 6 in Wang et al. (2010). Furthermore the weights of the kernels fitted to the available observations can produce abnormal BRDF shapes at very large solar zenith angles and the retrievals are not recommended for solar zenith angles over 70°. In producing accurate NDHDs from the MODIS BRDF product, we therefore need to pay attention to the BRDF shape produced by RTLSR.

The RTLSR model fails to accurately reproduce the sharp hotspot close to the sun's direction as observed by POLDER (Maignan et al., 2004). As POLDER sometimes directly observes the surface near the hotspot, its observations are used as the basis for evaluating the accuracy of the hotspot reconstructed from MODIS observations by RTLSR. While the fits are often quite good, Fig. 1 shows an extremely poor example where POLDER-3 observations were fitted by the MODIS RTLSR model. The BRDF curve for the NIR band in this example is dominated by the Ross-Thick kernel: the darkspot exists but the hotspot is weak; the highest BRF is in the hotspot in the observations but the RTLSR curve shows continuous increase of the BRF with θ_v on the principal plane beyond the hotspot. The hotspot BRF in the BRDF curve for the red band in this example is the largest BRF on the principal plane but it is also underestimated (Fig. 1). The darkspot in the red band can be found in the POLDER data but is not well simulated by RTLSR i.e. continuous decrease in BRF with increasing θ_v in the forward scattering direction. Therefore the magnitude of the hotspot produced by MODIS BRDF kernels must be corrected for the purpose of accurate retrievals of NDHD and CI.

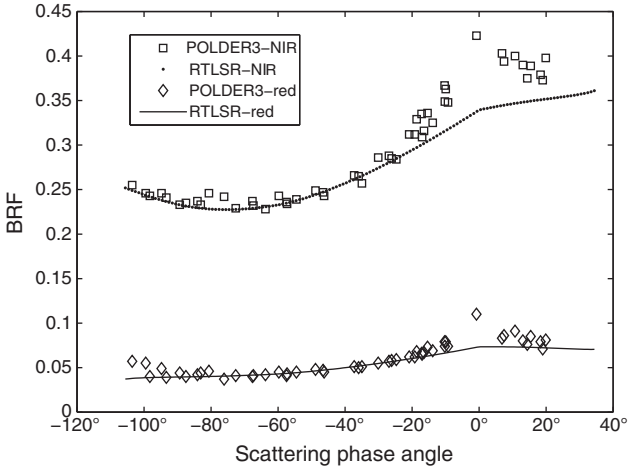

Fig. 1. Fitting POLDER-3 data using the MODIS RTLSR model (an extreme example for a closed broad-leaved forest). The hotspot reproduced by the model is much too small compared with POLDER data. The pixel's geographic coordinates are (64.03 N, 157.23 E); NDVI is 0.69; data are acquired in July 2006. The maximum BRFs in NIR and red bands from POLDER3 are 0.423 and 0.110, respectively; the hotspot BRFs from RTLSR in NIR and red bands are 0.34 and 0.0734, respectively. In fitting the data to RTLSR, RMSE for NIR is 0.010, and RMSE for red is 0.005.

Whereas the minimum BRF in the forward scattering direction is easily found from multi-angular measurements because the BRF near the darkspot changes only slowly with angle until a high θ_v where the bowl shape of the BRF may exist, a minimum in RTLSR model in the forward scattering direction cannot always be found for the given three parameters and a specific θ_s, as described above. For application of the algorithm of Chen et al. (2005) to MODIS data, a surrogate "minimum BRF" from the RTLSR model must be defined at an arbitrary θ_s associated with a fixed θ_v to compensate in situations with missing darkspots. We still call this surrogate minimum BRF the darkspot in the following text unless specified otherwise. The accuracy of darkspot BRF is therefore influenced by the method used to choose θ_s and θ_v.

3.1.2. Issue two: The hotspot BRF can be underestimated when the exponential approximation (Chen and Cihlar 1997) is used to extrapolate to the hotspot

The POLDER-3 data have multi-angular observations which contain data very close to the hotspot direction (albeit at a coarser spatial resolution), and they are used to correct the MODIS hotspot in this study. BRFs at the exact hotspot direction rarely exist for the POLDER-3 data. However, by fitting the BRFs near the hotspot according to a specific hotspot model, the exact hotspot can be found from extrapolation (Chen & Cihlar, 1997; Maignan et al., 2004). For example, Chen and Leblanc (1997) developed a hotspot kernel based on the gap size distribution theory. The hotspot kernel function is then approximated to an exponential function by Chen and Cihlar (1997):

$$F(\xi) = C_1 e^{-(|\xi|/\pi)C_2} \tag{18}$$

where C_1 determines the magnitude of the hotspot, and C_2 controls the width of the hotspot. It must be emphasized that (1) as a function of $|\xi|$, the hotspot kernel is symmetrical around its center ($\xi = 0°$) on the principal plane, and it describes only the hotspot component of the total BRF, but not the total BRF around the hotspot. The hotspot BRF has been approximated by directly using this hotspot kernel with some success and uncertainty (Chen et al., 2005; Pisek et al. 2010b; Simic & Chen, 2008). However, if the hotspot kernel is directly applied to the total BRF, only one side of the BRFs around the hotspot can be used to find the full hotspot at a time because the hotspot BRF is unnecessarily symmetrical around the hotspot; and (2) the error caused by the exponential approximation is also dependent on the distribution of scattering phase angles ξ in the observations: when the BRFs around the hotspot are uniformly distributed along the principal plane (in some simulations, e.g. Fig. 11 in Simic and Chen (2008)), the error can be minor, however this condition rarely happens in reality. More common cases are that fewer observations exist around the hotspot and more observations are far from the hotspot. As a result of least square fitting, the RMSE can be very small but the extrapolated hotspot can be negatively biased because the shape of physically-based hotspot kernel gets progressively sharper moving toward the exact hotspot ($\xi = 0°$) than the exponential function.

The exponential function defined by the constant hotspot width parameter (C_2) assumes the canopy contains gaps of an average size, while in reality there is a gap size distribution over a large range (Chen & Cihlar, 1997), making the hotspot sharper closer to the actual hotspot direction. Below we propose a new method to approximate the BRF in the exact hotspot direction.

3.1.3. Issue three: MODIS-derived CI is dependent on θ_s

In the algorithm of Chen et al. (2005), the averaged CI dependence on the θ_s for the POLDER observations is supposed to be explained by the dependence of coefficients A and B on θ_s, but in fact it is not true for MODIS data (see Section 4.2). The θ_s dependence of errors can be propagated into NDHD. If NDHD for a given pixel is reproduced at the θ_s at local solar noon from the MCD43A2 product, which is changing with season and latitude, errors are introduced in the global CI map. We propose an optimized scheme for global mapping of CI based on evaluation in Section 4.4.

3.2. Approximation of POLDER-3 hotspot BRF

We propose the following procedure to estimate POLDER-3 hotspot BRF as a basis for correcting the MODIS hotspot.

(a) BRDF data screening
In the POLDER-3 BRDF database, only those BRDFs which have at least one observation within $|\xi|<=1.5°$ or at least five observations within $|\xi|<=5°$ are chosen. We set these criteria as strictly as possible to guarantee enough angular samples around the hot spot. After this screening, ~3000 POLDER-3 BRDFs are kept in further analysis.

(b) Fitting the Ross–Roujean model using BRF data with large angular distances from the hotspot ($|\xi|>40°$), in order to quantify the non-hotspot component of each BRDF.
In the Ross–Roujean combination (Roujean et al., 1992), the geometric scattering kernel is:

$$K_{geo}(\theta_s,\theta_v,\phi)=\frac{1}{2\pi}[(\pi-\phi)\cos\phi+\sin\phi]\tan\theta_s\tan\theta_v-\frac{1}{\pi}\left(\tan\theta_s+\tan\theta_v+\sqrt{\tan^2\theta_s\tan^2\theta_v-2\tan\theta_s\tan\theta_v\cos\phi}\right) \quad (19)$$

and the volume-scattering kernel is the Ross-Thick model as shown in Eq. (8). We choose the Ross–Roujean model because it basically ignores the hotspot effect (Chen & Cihlar, 1997; Roujean et al., 1992).
Given the fitted kernel coefficients F from Eq. (16), the BRF near the hotspot without the hotspot effect ($BRF_m(\xi)$) is then reproduced by the Ross–Roujean model.

(c) Deriving unexplained hotspot BRF by fitting the hotspot kernel function using the exponential equation (Eq. (18)).
The difference $\Delta BRF(\xi)=BRF(\xi)-BRF_m(\xi)$ approximates the shape of hotspot kernel. The coefficients C_1 and C_2 in Eq. (18) can be fitted based on $\Delta BRF(\xi)$, collected on several orbits over a target area. To allow accurate derivation of C_1 and C_2 through curve fitting, only $\Delta BRF(\xi)$ within $|\xi|<=12.5°$ are used in the regression. If the RMSE<0.007 and the maximum of $\Delta BRF(\xi)$ is less than or equal to C_1, we treat this as a successful fit; otherwise, we repeat the regression and record the RMSE using only the BRFs from the orbit which includes the minimum $|\xi|$ when the following constraints are satisfied: there are at least one BRF within $|\xi|<5°$ and at least three BRFs within $|\xi|<12.5°$, or there is at least one BRF within $|\xi|<2°$ and at least three BRFs within $|\xi|<20°$. All the tests are used to constrain the curve fitting and get high quality hotspot kernel parameters, because we found that C_1 will be underestimated unless there are enough samples very close to $\xi=0$.

(d) The final hotspot BRF is taken as the sum of the hotspot BRF produced by the Ross–Roujean model without the hotspot effect and hotspot kernel magnitude C_1 derived in step (c).

3.3. Correction of MODIS hotspot BRF

POLDER-3 hotspot BRFs (BRF_{POLDER}) found through acceptable kernel fitting (RMSE<0.01 for the red band and RMSE<0.02 for NIR band) in the first 18 GLC2000 land cover types are used to correct the MODIS hotspot BRFs (BRF_{MODIS}). For each POLDER-3 pixel, its corresponding MODIS BRDF parameters of 269 pixels (13∗13) in the red and NIR bands, having the closest acquisition date, are calculated to form two subsets of MODIS BRDF for the two bands, and averaged, respectively. Subsets with more than 25% of MODIS pixels having no valid values were excluded in further analysis. The remaining (~2500) MODIS BRDF parameters are mostly of high quality and all of them are used in the analysis (Section 4.1); a reprocessing by excluding the non-high quality data produces only indiscernible improvements.

The hotspot BRFs in the red and NIR bands at the same θ_s as the POLDER-3 hotspot in each MODIS subset are reproduced according to RTLSR BRDF model parameters, and averaged. The averaged Normalized Difference Vegetation Index (NDVI) at nadir view was also produced in the same way for each subset.

The corrected MODIS hotspot BRF, BRF_{MODIS_corr}, is approximated as

$$BRF_{MODIS\_corr}=BRF_{MODIS}+\Delta BRF_{HS} \quad (20)$$

where ΔBRF_{HS} is the difference between POLDER-3 and MODIS hotspot BRF, and to be parameterized by NDVI and θ_s (Section 4.1).

3.4. Derivation of MODIS CI

The BRDF can be reproduced from the MODIS BRDF parameter product for any geometry. The BRDF reproduced at the θ_s of the actual observations is supposed to be mostly error free; when the BRDF is reproduced at another θ_s, model error may be enlarged. To test how the derived CI can change with θ_s, we produced CI at different θ_s for site 30 (to be shown in Section 4.2). At each θ_s, methods to use a dynamic darkspot searching method (searching the minimum in the forward-scattering direction up to $\theta_v=60°$), and the fixed method (θ_v is chosen as the Ross kernel's darkspot angle) in deriving CI are also evaluated.

After the MODIS hotspot is corrected using Eq. (20) and the NDHD is calculated, the coefficients (A and B) calculated from the second-order polynomial fit of the tabulated relationship between CI and NDHD in Chen et al. (2005) is used to derive MODIS CI. The crown shapes of needle-leaved forests (land covers 4 and 5) are set to "Cone + cylinder", and the crown shapes of other land covers are set to "Ellipsoid" (Chen et al., 2005) according to the GLC land cover product.

Snow-free land pixels are selected by the MODIS Snow_BRDF_Albedo product. Any pixel with NDVI<0.1 (no enough vegetation fraction) or with $f_{vol}=f_{geo}=0$ (representing no clumping) is excluded. The minimum, the median or the mean value of CI from the seasonal trajectory is tested for representing the clumping in a year in the final product.

4. Result and evaluation

4.1. MODIS hotspot correction

For the red band, as shown in Fig. 2(a), it is found that the hotspot BRF from the MODIS RTLSR model is underestimated by ~16%. The relationship between MODIS RTLSR hotspot and POLDER-3 hotspot in this band is nonlinear: smaller MODIS RTLSR hotspot BRFs are relatively more underestimated. The difference between POLDER-3 and MODIS

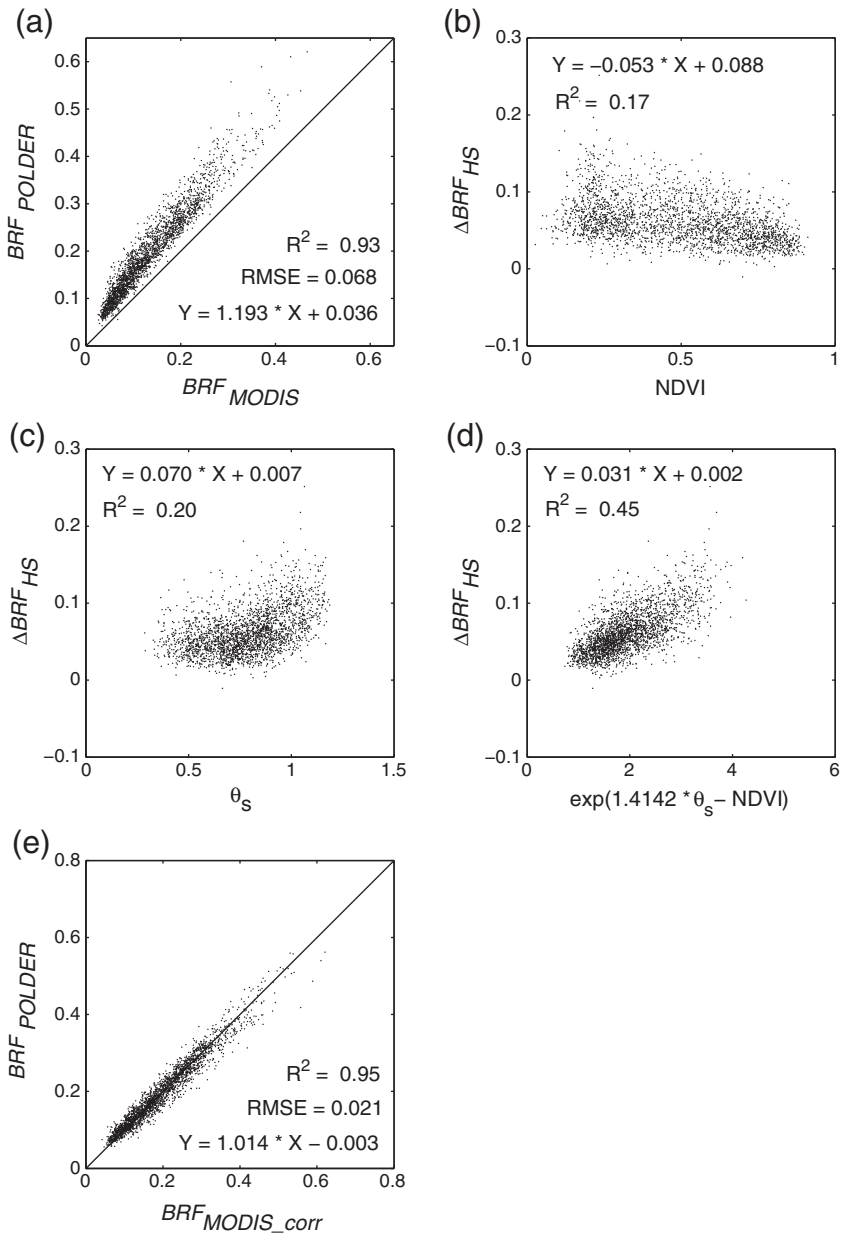

Fig. 2. Correction of MODIS RTLSR hotspot using POLDER-3 hotspot for the red band (samples = 2495). Panel (a) shows a scattering plot between the POLDER hotspot (BRF_{POLDER}) and the original MODIS RTLSR hotspot (BRF_{MODIS}); panel (b) shows a scattering plot between NDVI calculated from the MODIS RTLSR model and the difference between the two hotspots ($\Delta BRF_{HS} = BRF_{POLDER} - BRF_{MODIS}$); panel (c) shows a scattering plot between ΔBRF_{HS} and the θ_s when the hotspot is observed; panel (d) shows a scattering plot between ΔBRF_{HS} and a combined variable of NDVI and θ_s; and panel (e) shows a scatter plot between the POLDER hotspot and the MODIS RTLSR hotspot after the correction (BRF_{MODIS_corr}) using the relationship shown in panel (d): $BRF_{MODIS\_corr} = BRF_{MODIS} + BRF_{HS}$, and $BRF_{HS} = 0.031 \cdot \exp(1.4142 \cdot \theta_s - NDVI) + 0.002$. P values<<0.01 in all panels.

RTLSR hotspot BRF, ΔBRF_{HS}, is shown to be negatively correlated with the NDVI at nadir direction (Fig. 2b) and positively correlated with θ_s (Fig. 2c). By combining the θ_s and NDVI into one index (Fig. 2d), the ΔBRF_{HS} is approximated as

$$\Delta BRF_{HS} = 0.031 \cdot \exp(1.4142 \cdot \theta_s - NDVI) + 0.002. \quad (21)$$

After applying Eq. (21) to Eq. (20), the MODIS RTLSR hotspot BRF and POLDER-3 hotspot BRF in Fig. 2e are close to 1: 1 line.

For the NIR band, the correction of its MODIS RTLSR hotspot BRF is similar to the red band except that: the MODIS RTLSR hotspot BRF in NIR band is underestimated by ~14%; ΔBRF_{HS}, is found to be positively correlated to NDVI; and

$$\Delta BRF_{HS} = 0.006 \cdot \exp(2.3662 \cdot \theta_s + NDVI) + 0.028. \quad (22)$$

The result for the correction of RTLSR hotspot BRFs in red and NIR is summarized in Table 3.

4.2. CI sensitivity to θ_s, darkspot searching method, and the land cover

Fig. 3 illustrates how the MODIS-derived CI is influenced by θ_s, darkspot searching method, and land cover accuracy. In this example, the BRDF parameters for the red and NIR bands are the yearly averages from high quality values of the 8-day MODIS BRDF product for site 30 (in Table 1). The forest is composed of needle-leaved trees but we also tried to get CI assuming that it is a broad-leaved forest to test the importance of using a land cover map. After the hotspot is corrected, the CIs still show strong dependence on θ_s (except for cone + cylinder, red band) and the dependences are in different (increasing or decreasing) patterns. The NIR band shows stronger

Table 3
Summary of result for correcting MODIS RTLSR hotspot using POLDER-3 hotspot (N = 2495 for red band and N = 2448 for NIR band; p values < 0.01). The letters a to e are corresponding to the orders of panels in Fig. 2.

No.	Equation	R^2	RMSE
Red band			
a	$BRF_{POLDER} = BRF_{MODIS} * 1.193 + 0.036$	0.93	0.068
b	$\Delta BRF_{HS} = -0.053 * NDVI + 0.088$	0.17	
c	$\Delta BRF_{HS} = -0.070 * \theta_s + 0.007$	0.20	
d	$\Delta BRF_{HS} = -0.031 * X + 0.002$ $X = \exp(1.4142 * \theta_s - NDVI)$	0.45	
e	$BRF_{POLDER} = BRF_{MODIS\_corr} * 1.014–0.003$ $BRF_{MODIS\_corr} = BRF_{MODIS} + \Delta BRF_{HS}$	0.95	0.021
NIR band			
a	$BRF_{POLDER} = BRF_{MODIS} * 1.162 + 0.032$	0.80	0.101
b	$\Delta BRF_{HS} = 0.077 * NDVI + 0.054$	0.13	
c	$\Delta BRF_{HS} = -0.140 * \theta_s - 0.019$	0.29	
d	$\Delta BRF_{HS} = 0.006 * X + 0.028$ $X = \exp(2.3662 * \theta_s + NDVI)$	0.38	
e	$BRF_{POLDER} = BRF_{MODIS\_corr} * 0.981 + 0.008$ $BRF_{MODIS\_corr} = BRF_{MODIS} + \Delta BRF_{HS}$	0.87	0.037

dependence on θ_s than the red band. Accurate CI cannot be derived unless a correct crown shape is used. We tested the dynamic darkspot searching method and the fixed method. The fixed method (lines with down-triangles) produces slightly higher CI than the dynamic method (lines with up-triangles), but their patterns are very similar (lines are parallel).

4.3. Seasonal trajectory of CI

Given the multi-temporal observations from POLDER, a representative CI is chosen by searching the minimum CI from its seasonal trajectory in the global map (Chen et al., 2005). The same technique can be hardly applied to MODIS data, as the minimum CI in the MODIS CI trajectory generally contains extreme fluctuations. For example, the seasonal trajectories of CI for an evergreen forest site 30 (Table 1) for the two bands produced by using only high quality data are shown for snow-free days in Fig. 4. There appears to be an abnormal period with low CI values between day of year (DOY) 160 and DOY 190. With the irregular fluctuations of the derived CI values, no obvious seasonal trajectory can be discerned. In this example, the minimum CI does not reflect the maximum level of clumping but noise.

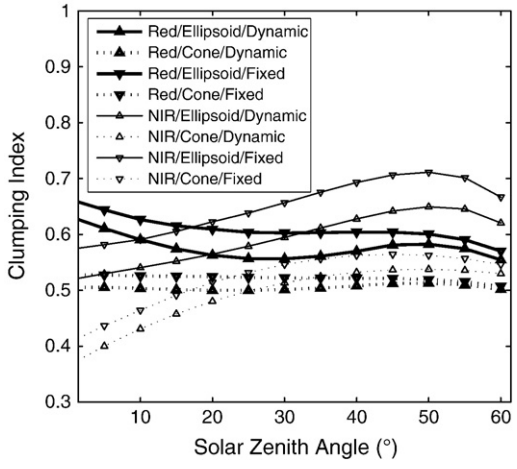

Fig. 3. The CI dependence on θ_s, land cover, and the darkspot searching method for site 30. The kernel coefficients are 0.0478, 0.0343, and 0.0098, for red band, and 0.2564, 0.1020, and 0.0452 for NIR band (yearly average).

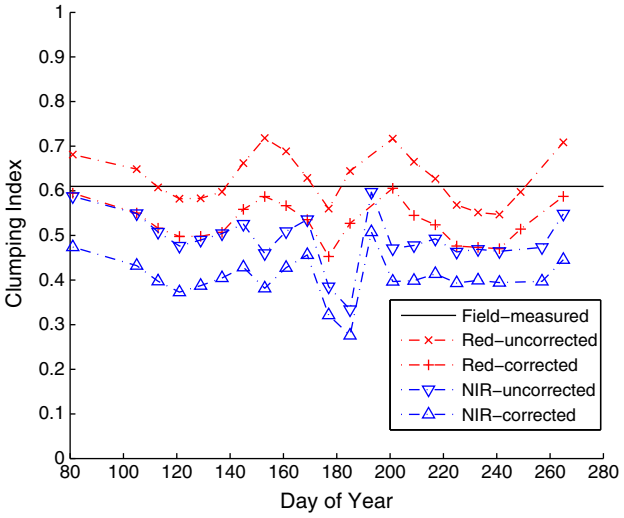

Fig. 4. Seasonal trajectories of CIs for site 30 (snow-free and high-quality data are used, θ_s is set to 0°, and θ_v at darkspot is set to 47.7°).

4.4. The evaluation of MODIS-derived CI

In order to evaluate the MODIS-derived CI, the BRDF parameters for the 38 forest sites are extracted from the MODIS product for every 8 days. These BRDF parameters from the 38 sites were used to reproduce the hotspot and darkspot BRFs to derive CI with the method described in Section 3.

Various θ_s, darkspot searching methods, and averaging methods have been tested to derive CI in comparison with ground measurements. The median values of MODIS-derived seasonal trajectories of CI for the 38 sites show a slightly higher correlation with field measurements than the mean values for both red and NIR bands. We also do not recommend using the minimum CI to represent yearly CI in the global map as it is frequently contaminated by noise.

The crown shape can explain a large proportion of variance in the CI algorithm. The NDHD and CI relationships have been regressed separately for different crown shapes (Chen et al., 2005). Therefore, we should check the correlation between field and satellite measurements for each crown shape group for accurate evaluation.

For example, for the needle-leaved forest group, we found that R^2 between MODIS-derived CI and field-measured $\Omega(\theta)$ will decrease with increasing θ_s (same result as found by Chen et al., 2005), but R^2 will increase with decreasing darkspot θ_v, causing a decrease in the dynamic range of MODIS-derived CI.

It should also be noted that the kernel coefficient f_{iso} plus ΔBRF_{HS} is the hotspot BRF when $\theta_s = \theta_v = 0$, and the hotspot BRF is free from the uncertainties in the other two kernel coefficients as $K_{vol} = K_{geo} = 0$ at nadir; as shown in Eqs. (21) and (22), the ΔBRF_{HS} dependence on θ_s disappears at nadir and the nadir NDVI is also the NDVI at the hotspot. The BRDF model fitted to observations is supposed to reproduce the best hotspot BRF at the θ_s at which observations are made, and the hotspot BRF at nadir is generally not observed by MODIS and thus may be considered as extrapolation from observations at other angles using the fitted model. However, given the CI dependence on θ_s described in Section 4.2, using a fixed θ_s is a way to minimize such dependence. As a result of our comprehensive investigation, we propose the following scheme for processing global data: θ_s is set to 0°, θ_v for darkspot is fixed to 47.7°, and the median CI from the high quality data within the snow-free period of a year is used to represent the CI in the global map (if the amount of high quality CIs is less than 5, all the CI is used to get median CI). 47.7° is the θ_v of darkspot for Ross-Thick kernel when $\theta_s = 0°$. We choose a fixed θ_v for the darkspot to reduce computational burden in global data processing. Model simulations show that NDHD at smaller θ_s correlates better with CI

than that at larger θ_s (Chen et al., 2005), and this is further confirmed by our evaluation.

The evaluation result for the proposed scheme is shown in Fig. 5. It can be seen that the CIs in each panel in Fig. 5 are separated into two clusters, one is for needle-leaved forest, and one for broad-leaved forest. For both bands in Fig. 5, more than 50% of the variance in CIs can be explained. The dynamic range of MODIS-derived CI is smaller than field-measured $\Omega(\theta)$. The MODIS CI is smaller than field-measured $\Omega(\theta)$, and the difference is proportional to the value of CI. It should be emphasized that only the MODIS CIs in the needle-leaved forest group in red band are shown to be significantly correlated to the field-measured $\Omega(\theta)$ with R^2 larger than 0.5. The regressed slope for needle-leaved forest group in red band is comparable to the slope for all forest types, while the slope in NIR band is much smaller. There were only 10 broad-leaved forest sites used in the validation, which are too few for a reliable validation. The dynamic range of field-measured $\Omega(\theta)$ for most of these sites (9 out 10) is also too small to produce a significant correlation.

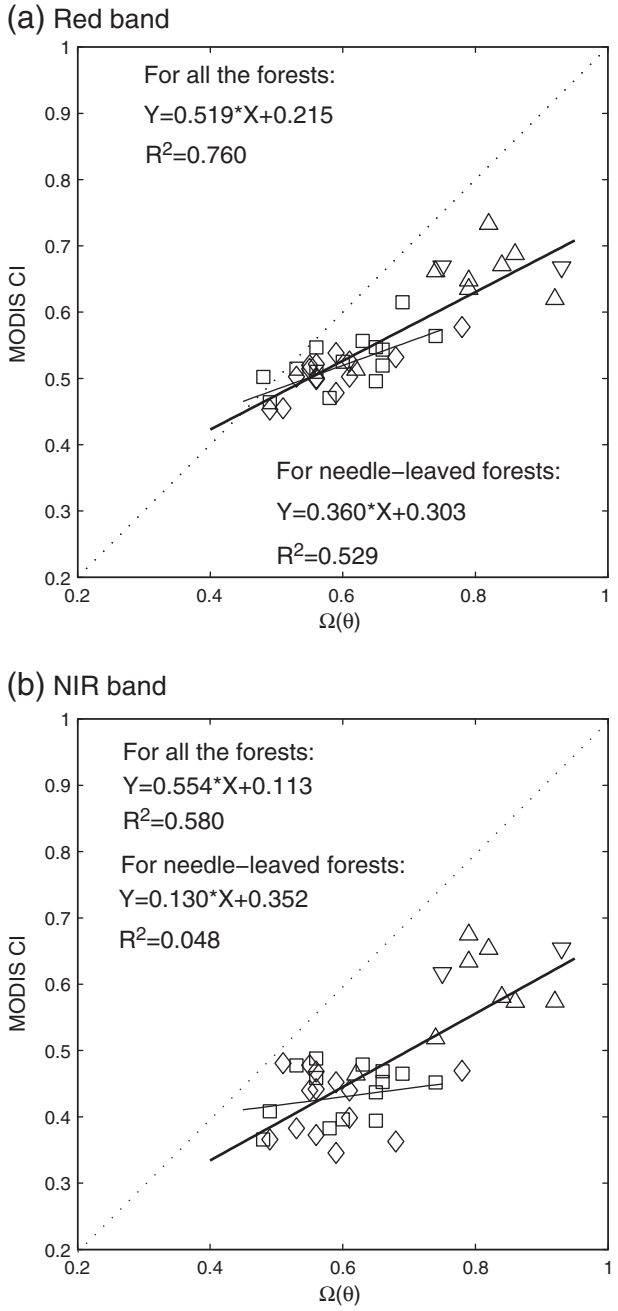

Fig. 5. Evaluation of MODIS CI using field measurements for the proposed scheme. Triangles denote the broad-leaved forests, and the squares and diamonds denote the needle-leaved forests; the surrogate pixels are marked diamonds and down-triangles. The thinner regression lines are for needle-leaved forests, and the thicker regression lines are for all the sites.

4.5. Global CI map

The global map of CI at a 500 m resolution (Fig. 6) is derived using the red band of MODIS BRDF parameters product in 2006 and the method/parameters applied in Fig. 5(a). In the global CI map, the CI of needle-leaved forest (in dark green) is distinctly different from the CI of other land cover types as the CI is mostly controlled by the crown shapes. The evergreen broad-leaved forest along the equator (in Amazon and central Africa) is distinguished by the lighter green color. The CI of desert is masked out (otherwise the value is very close to 1). Moving away from deserts, the CI for other land covers gradually changes from yellow to brown colors, indicating increasing levels of clumping.

Comparing the MODIS-derived CI with the CI map derived from POLDER-3 data (Pisek et al., 2010b), we found the following differences: (1) the MODIS-derived CI value is systemically lower than the POLDER-3 CI value; (2) the POLDER-3 CI for many needle-leaved forests (assuming that the GLC2000 is correct) such as in boreal forests, south-east US, and south-east China is not consistently lower than other cover types; this is possibly caused by the error in the land cover map at 6 km resolution, in which non-dominant needle-leaved forest types are replaced by other dominant cover types; such problem is avoided in the MODIS map; (3) the POLDER-3 CI for broad-leaved and mixed forests in northern-eastern US shows larger differences from the adjacent land cover types than the MODIS-derived CI.

Fig. 7 shows an example of a case where all the 500 * 500 pixels are assigned non-needle-leaved forest land covers by GLC2000, so the CI is only dependent on the NDHD. The pattern of the land cover distribution (e. g., the contour line of broad-leaved, evergreen forest, land cover 2) shown in Fig. 7a can be easily discerned from the MODIS-derived CI map (Fig. 7b) with consistently lower CI than its contiguous land covers. The result suggests that the hotspot correction improves the differentiation of clumping between cover types.

The mean CI and its one standard deviation for each land cover from Fig. 6 are shown in Table 2. The evergreen needle-leaved forest has the lowest CI (0.53), followed by deciduous needle-leaved forest (0.57) and evergreen broad-leaved forest (0.66). There is not much difference in CI (~0.7) of other land cover types (including variations in tree cover–shrub, herbaceous plants, grass, and cropland all have CI values of about 0.75).

Fig. 8 shows that the MODIS-derived CI decreases nearly linearly with increasing percent tree cover in the VCF product for most land cover types. The magnitude of the decrease is dependent on the land cover type: ~0.02 for land cover 1 to 10 and ~0.05 for land cover 11 to 18. The decreasing trend is reasonable because the CI of non-tree covers dominates in the mixed pixel when percent tree cover is lower.

5. Discussion and uncertainty analysis

5.1. Cross-calibration and scale effect between POLDER-3 and MODIS

Recent cross-calibration between POLDER-3 and MODIS show that BRFs of the two sensors are in good agreement (close to or better than 1%), so no further cross-calibration is implemented for hotspot BRF in

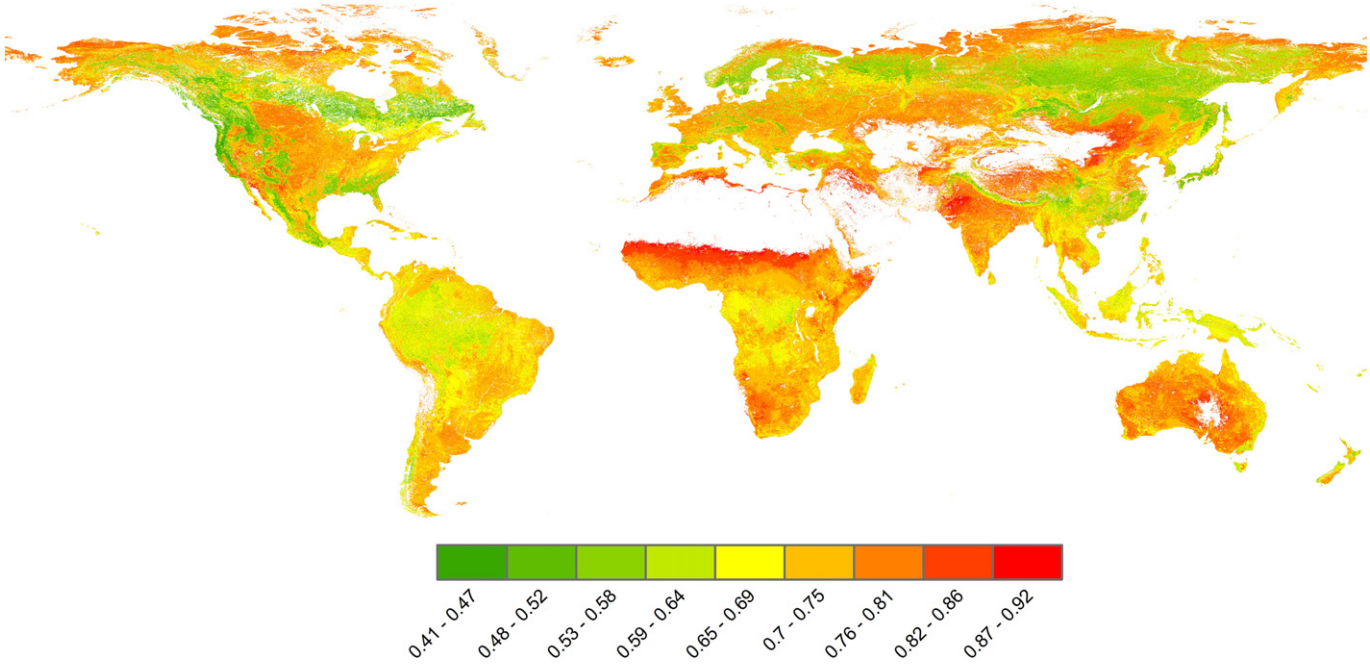

Fig. 6. Global map of MODIS-derived clumping index in 500 m resolution for 2006.

this study (Bouvet, 2007; Gamet et al., 2010). The regression coefficients for the red and NIR bands in Table 2 of Chen et al. (2005) are derived for POLDER using the 5-Scale model (Chen & Leblanc, 1997, 2001). Neither of these coefficients is corrected for MODIS due to the good agreement between MODIS and POLDER in these two bands.

In this study, we did not correct for the scale effect on the hotspot magnitude between the POLDER-3 and MODIS observations. The scale effect depends on both the spatial heterogeneity of the pixel of interest and the algorithm used (Chen, 1999). Given the fact that homogenous pixels are selected for cross-calibration of the hotspot magnitude between POLDER-3 and MODIS, the scale effect on the hotspot magnitude between 500 m and 6 km resolution may be very small due to the minor change in semivariance at pixel sizes much larger than the scale of surface heterogeneity (Roman et al., 2009; Woodcock & Strahler, 1987). As radiative fluxes from small pixels within a large grid (pixel) are linearly additive in obtaining the total radiative flux for the grid, the hotspot or darkspot obtained from averaging MODIS pixels within a grid would be the same as a single hotspot or darkspot measurement over the grid.

5.2. Fluctuations in seasonal trajectory of CI

There are no plausible physical reasons to explain most of the short-term fluctuations of the derived CI value during the growing season (Fig. 4) except for measurement noise. However, some of the fluctuations could be related to vegetation phenology. Chen (1996) and Sprintsin et al. (2011) show that the effect of foliage clumping at scales larger than the shoots is invariant with season (for needle-leaved forest). Ryu et al. (2010a) show that there is strong seasonal variation for temperate deciduous forest (Harvard forest) and CI is variable (caused by invasive plant infestation). It is interesting to note that the fluctuations of the CI values derived from red and NIR bands occur almost simultaneously (or one time-step different) and the amplitude of the CI fluctuations in the NIR band is larger than those in the red band. This simultaneous change of CI in both bands implies that the algorithm effectively captured the temporal trajectory of CI. The one time-step difference could be caused by the smoothing effect of data screening of the MODIS BRDF algorithm because the BRDF model parameters are retrieved using BRFs collected within 16 days. In this study we treated such fluctuations as information but some extreme minimum CI may not represent the maximum clumping level in the usual condition. While it is reasonable to use the median value to represent an average clumping for needle-leaved stands, the median value may underestimate the clumping effect for deciduous forest during the peak growing season when the foliage is densest.

5.3. Importance of the land cover map

The land cover (and therefore the forest species) map is shown to be very important for the accuracy of CI because it decides which crown shape to be used in the algorithm for each pixel. The land cover determined the basic pattern of the CI map: the needle-leaved forest is remarkably differentiated from the other land cover types with the lowest CI. In the evaluation (Figs. 5), two distinct clusters are dominated by the land cover: once the land cover is correct, the R^2 values between MODIS-derived and field-measured CIs are higher than 0.5 (as shown in Figs. 5, the thicker line), even though R^2 is less than 0.1 within each cluster, implying that the correct land cover itself can explain most of the variance in the CI map, otherwise CI can be seriously biased by using a wrong land cover type. Caution should be taken for the misclassification in GLC 2000 land cover map as their errors can be propagated into the CI map.

5.4. Limitation in site validation data

We realize that there are not enough sites for rigorous evaluation of the global CI map. The sites chosen in this study are mainly dense forests, so any conclusions drawn from the evaluation would apply reliably to dense forests only. The evaluation has been taken with precaution as we used surrogate pixels from adjacent pure pixels to match TRAC measurements.

5.5. Explanation of the CI difference between bands

Chen et al. (2005) exploits the contrast between hotspot and darkspot BRFs to map CI, relying on the fact that more clumped canopies cast more shadows (under the condition that the canopy cover is

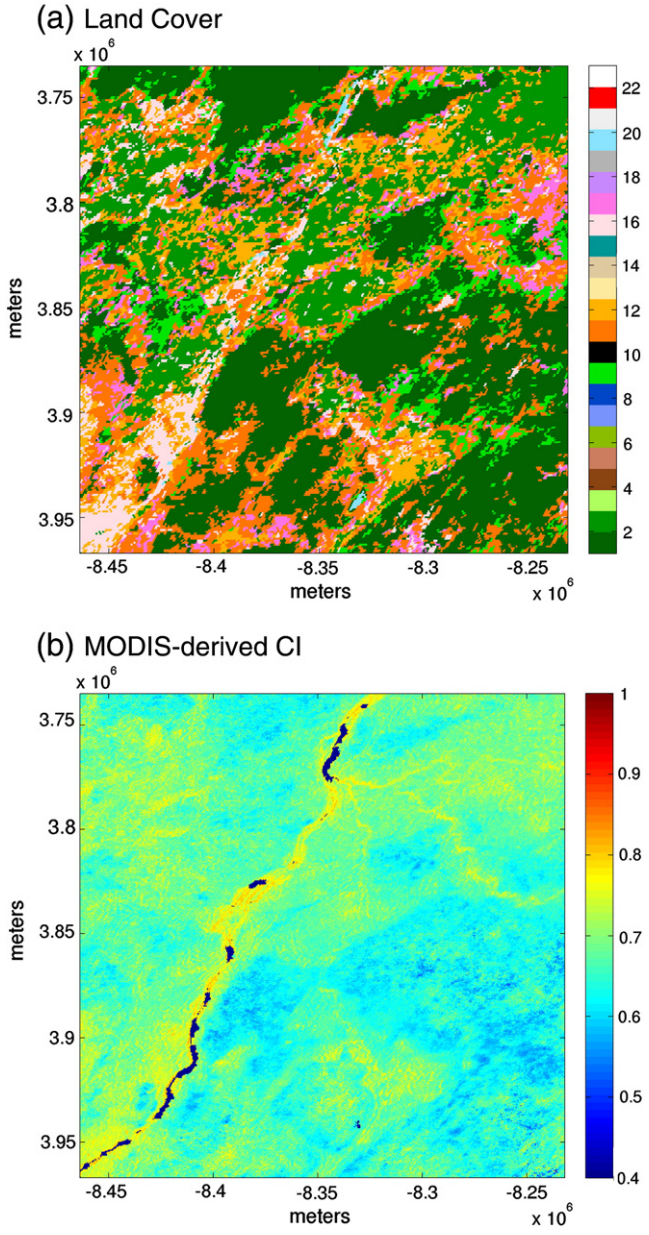

Fig. 7. Comparison of MODIS-derived clumping index map with land cover. The geographical coordinates are (14.22 N, 106.25E). All the land covers in the 500∗500 pixels are broad-leaved forests. The CI clearly shows the pattern of evergreen broad-leaved forest in land cover map.

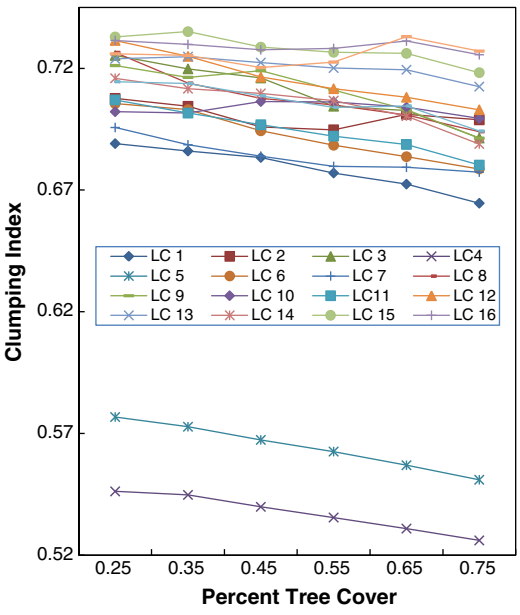

Fig. 8. CI decreases with the increase of percent tree cover. In the legend, LC denotes "GLC Land Cover".

greater than 25%). Theoretically, BRF in red band is more affected by the canopy structure than NIR reflectance because NIR has strong multi-scattering that reduces the contrast between hotspot and dark-spot, but in satellite remote sensing, the red band is often more influenced by atmospheric contamination than the NIR band. NIR band was also favored in mapping CI due to its smaller contamination by background reflectance. Simulations by the 5-Scale model show that the NIR band is slightly better than the red band in retrieving CI under the condition that the BRDF curve is free of atmospheric contamination (Chen et al., 2005).

In this study, we have chosen the MODIS red band in producing the global CI map. We could also use the NIR band because this band was favored over the red band in mapping CI in savanna woody cover where the multi-scattering effect is less than that of the dense forests (Hill et al., 2011) or in areas where the atmospheric effect is persistent (Pisek et al., 2011a). The MODIS CI derived from the NIR BRF showed smaller values than the red band (Figs. 4 and 5). This could be due to errors in simulating the directional variation of multiple scattering in the plant canopy with the 5-Scale model (Chen & Leblanc, 1997, 2001) used to develop our clumping algorithm. Thus, considering the good quality of atmospheric correction of MODIS product (Vermote et al., 2002) and using the indications given in Fig. 5, we chose the red band over NIR band for producing the MODIS CI map. We understand that there are uncertainties in the long data-processing chain from 5-Scale modeling, CI algorithm development, BRDF retrieval, hotspot correction, to global CI mapping. We expect that the accuracy of the CI map should be further validated and the sensitivities of CI to different land covers should be evaluated using a large amount of field measurements.

5.6. Uncertainty in ground measurement of clumping

TRAC-measured $\Omega_e(\theta)$ generally increases with θ_s. In Chen (1996), TRAC-measured $\Omega_e(\theta)$ at $\theta_s = 39°$ is proposed to represent the average Ω_e. However, the TRAC measurements assembled by Pisek et al. (2011a) may be made at very different θ_s but the θ_s at which measurements were made is not always available in the publications, making it impossible to do further calibration. In this study, directional $\Omega_e(\theta)$ divided by γ_e has to be compared to an average CI produced by MODIS data. This is one source of error in our evaluation. The accuracy of γ_e is very sensitive to $\Omega(\theta)$; while Walcroft et al. (2005) found that the γ_e increases with height at New Zealand site (#10), some sites have no γ_e or use an assumed γ_e.

In this study we found that the CI values derived from MODIS data after the rigorous hotspot correction become consistently smaller than ground-measured CI. Satellite measurements respond to the structural effects near the top, while ground measurements may be biased by the lower vegetation layers. In our CI algorithm development (Chen et al., 2005), clumping was determined from the true LAI input and the resulting gap fraction simulated by the geometrical optical model 5-Scale, therefore the algorithm should allow the correct retrieval of the stand average clumping of the leaves. However, we are also aware of the limitation of the 5-Scale model in explaining the multiple scattering (Chen & Leblanc, 1997, 2001). In moderate to dense forest stands, TRAC measurements near the ground surface may considerably underestimate the overall canopy-level clumping

effect (i.e. producing too large CI values). This is because the large gaps between tree crowns at upper levels of the canopy may not be all measured near the ground due to obscurity by lower branches; for example, one branch separates one large gap into two gaps, this would not change gap fraction significantly, but it changes the gap size distribution which is used to estimate Ω_e by TRAC and leads to a larger Ω_e (Chen & Cihlar, 1995a). The field measurements of the clumping index may also often be influenced by the presence of the understory at forest sites, making the measurement positively biased because the grass/shrub understory is generally more random than the tree overstory. Ryu et al. (2010a) also recently reported that Ω_e calculated from the current methods from the field measurements might be overestimated (see also Pisek et al., 2011b). We therefore suggest that our ground CI measurement techniques need to be further developed to address the difference between $\Omega(\theta)$ and MODIS-derived CI.

6. Conclusion

The MODIS BRDF parameter product in 500 m resolution has been utilized as an important data source to derive a global clumping index map, and therefore the spatial resolution of an existing global CI map at 6 km derived from the POLDER data is greatly improved. This improvement is critical in global LAI mapping which is generally done at 1 km resolution (Garrigues et al., 2008).

The most critical technical issue in using MODIS data for CI mapping is that MODIS does not observe near the hotspot and the angular kernels used to construct the MODIS BRDF product do not include the complete hotspot physics and consistently underestimate the hotspot. We have therefore developed a method to correct this hotspot underestimation based on the solar zenith angle at the time of MODIS observation and nadir NDVI. POLDER-3 measurements near the hotspot are extrapolated to the hotspot using an exponential function and used as the basis for MODIS hotspot correction.

Red band reflectance is more affected by the canopy structure than NIR reflectance. In this study, MODIS red band data are found to be better than the NIR data to derive CI in comparison with ground-measured CI. This is opposite to previous finding for POLDER data which favors the use of NIR data. This presumably indicates that MODIS atmospheric correction has made the red band data more reliable.

MODIS-derived CI values after the hotspot correction are found to be consistently lower than available ground data of directional CI ($\Omega(\theta)$ defined in Section 1) with reasonably uniform covers within the corresponding MODIS pixels. The difference may be due to our insufficient understanding and modeling of CI from satellite and/or ground and suggests that further studies are needed to address the difference. In spite of this limitation, our study shows that it is promising to map CI routinely and reliably from multi-angular satellite measurements in the future.

Acknowledgment

The POLDER-3/PARASOL BRDFs databases have been elaborated by the LSCE, and provided by the POSTEL Service Centre. We thank Kate Liss for data processing. The research was supported by a project (2010CB950700) founded by the Global Change Program of the Chinese Ministry of Science and Technology and a Discovery Grant to J. M. Chen from the Natural Science and Engineering Research Council of Canada. Jan Pisek is supported by the funding from the FP7-Marie Curie Actions programme, Estonian Science Foundation grant no. ERMOS32. Crystal B. Schaaf and Alan H. Strahler have been supported by NASA Grant: NNX08AE94A. The clumping index map shown in the paper will be available upon request. The authors would like to thank two anonymous reviewers whose constructive comments led to a better presentation of our research methods and results.

References

GLC (2003). Global land cover 2000 database. European Commission, Joint Research Centre, 2003. http://bioval.jrc.ec.europa.eu/products/glc2000/glc2000.php

Baldocchi, D. D., & Harley, P. C. (1995). Scaling carbon dioxide and water vapour exchange from leaf to canopy in a deciduous forest. II. Model testing and application. *Plant, Cell & Environment*, *18*, 1157–1173.

Bouvet, M. (2007). Intercomparison of multispectral imagers over natural targets. *IGARSS: 2007 IEEE International Geoscience and Remote Sensing Symposium*, *vols 1–12*. (pp. 2653–2664).

Bréon, F. M., Fédèle, E., Maignan, F., & Lacaze, R. (2007). A database of directional reflectance signature (GLC2000) with an analysis tool. *A-Train Symposium. Lille*.

Chen, J. M. (1996). Optically-based methods for measuring seasonal variation of leaf area index in boreal conifer stands. *Agricultural and Forest Meteorology*, *80*, 135–163.

Chen, J. M. (1999). Spatial scaling of a remotely sensed surface parameter by contexture. *Remote Sensing of Environment*, *69*, 30–42.

Chen, J. M., & Black, T. A. (1992). Foliage area and architecture of plant canopies from sunfleck size distributions. *Agricultural and Forest Meteorology*, *60*, 249–266.

Chen, J. M., & Cihlar, J. (1995). Plant canopy gap-size analysis theory for improving optical measurements of leaf-area index. *Applied Optics*, *34*, 6211–6222.

Chen, J. M., & Cihlar, J. (1995). Quantifying the effect of canopy architecture on optical measurements of leaf-area index using 2 gap size analysis-methods. *IEEE Transactions on Geoscience and Remote Sensing*, *33*, 777–787.

Chen, J. M., & Cihlar, J. (1997). A hotspot function in a simple bidirectional reflectance model for satellite applications. *Journal of Geophysical Research-Atmospheres*, *102*, 25907–25913.

Chen, J. M., Govind, A., Sonnentag, O., Zhang, Y. Q., Barr, A., & Amiro, B. (2006). Leaf area index measurements at Fluxnet-Canada forest sites. *Agricultural and Forest Meteorology*, *140*, 257–268.

Chen, J. M., & Leblanc, S. G. (1997). A four-scale bidirectional reflectance model based on canopy architecture. *IEEE Transactions on Geoscience and Remote Sensing*, *35*, 1316–1337.

Chen, J. M., & Leblanc, S. G. (2001). Multiple-scattering scheme useful for geometric optical modeling. *IEEE Transactions on Geoscience and Remote Sensing*, *39*, 1061–1071.

Chen, J. M., Liu, J., Leblanc, S. G., Lacaze, R., & Roujean, J. L. (2003). Multi-angular optical remote sensing for assessing vegetation structure and carbon absorption. *Remote Sensing of Environment*, *84*, 516–525.

Chen, J. M., Liu, J., Leblanc, S. G., Roujean, J. L., & Lacaze, R. (2001). Utility of multi-angle remote sensing for terrestrial carbon cycle modeling. *Proceedings of the 8th International Symposium on Physical Signatures and Measurements in Remote Sensing, Aussois, France* (pp. 249–258). Toulouse, France: CNES.

Chen, J. M., Menges, C. H., & Leblanc, S. G. (2005). Global mapping of foliage clumping index using multi-angular satellite data. *Remote Sensing of Environment*, *97*, 447–457.

Chen, J.M., Mo, G., Pisek, J., Deng, F., Ishozawa, M., & Chan, D. (in press). Foliage clumping index as an important structural parameter for estimating global terrestrial gross primary productivity. *Global Biogeochemical Cycles*.

Chen, J. M., Pavlic, G., Brown, L., Cihlar, J., Leblanc, S. G., White, H. P., et al. (2002). Derivation and validation of Canada-wide coarse-resolution leaf area index maps using high-resolution satellite imagery and ground measurements. *Remote Sensing of Environment*, *80*, 165–184.

Chen, J. M., Rich, P. M., Gower, S. T., Norman, J. M., & Plummer, S. (1997). Leaf area index of boreal forests: Theory, techniques, and measurements. *Journal of Geophysical Research-Atmospheres*, *102*, 29429–29443.

Chen, Q., Baldocchi, D., Gong, P., & Dawson, T. (2008). Modeling radiation and photosynthesis of a heterogeneous savanna woodland landscape with a hierarchy of model complexities. *Agricultural and Forest Meteorology*, *148*, 1005–1020.

Duthoit, S., Demarez, V., Gastellu-Etchegorry, J. P., Martin, E., & Roujean, J. L. (2008). Assessing the effects of the clumping phenomenon on BRDF of a maize crop based on 3D numerical scenes using DART model. *Agricultural and Forest Meteorology*, *148*, 1341–1352.

Gamet, P., Fougnie, B., & Lacherade, S. (2010). Calibration of PARASOL over desert sites: Cross-calibration with POLDER and MODIS sensors. *International Symposium on the A-Train Satellite Constellation 2010*. USA: New Orleans.

Garrigues, S., Lacaze, R., Baret, F., Morisette, J. T., Weiss, M., Nickeson, J. E., et al. (2008). Validation and intercomparison of global leaf area index products derived from remote sensing data. *Journal of Geophysical Research-Biogeosciences*, *113*.

Gonsamo, A., & Pellikka, P. (2008). Methodology comparison for slope correction in canopy leaf area index estimation using hemispherical photography. *Forest Ecology and Management*, *256*, 749–759.

Hansen, M., DeFries, R., Townshend, J. R., Carrol, M., Dimiceli, C., & Sohlberg, R. (2007). *Vegetation continuous fields MOD44B, 2000 percent tree cover, collection 4.* In: University of Maryland.

Hansen, M. C., DeFries, R. S., Townshend, J. R. G., Carroll, M., Dimiceli, C., & Sohlberg, R. A. (2003). Global percent tree cover at a spatial resolution of 500 meters: First results of the MODIS vegetation continuous fields algorithm. *Earth Interactions*, *7*.

Hansen, M. C., DeFries, R. S., Townshend, J. R. G., Sohlberg, R., Dimiceli, C., & Carroll, M. (2002). Towards an operational MODIS continuous field of percent tree cover algorithm: Examples using AVHRR and MODIS data. *Remote Sensing of Environment*, *83*, 303–319.

Hapke, B., DiMucci, D., Nelson, R., & Smythe, W. (1996). The cause of the hotspot in vegetation canopies and soils: Shadow-hiding versus coherent backscatter. *Remote Sensing of Environment*, *58*, 63–68.

Hautecoeur, O., & Leroy, M. M. (1998). Surface bidirectional reflectance distribution function observed at global scale by POLDER/ADEOS. *Geophysical Research Letters*, *25*, 4197–4200.

Hill, M. J., Román, M. O., Schaaf, C. B., Hutley, L., Brannstrom, C., Etter, A., et al. (2011). Characterizing vegetation cover in global savannas with an annual foliage clumping index derived from the MODIS BRDF product. *Remote Sensing of Environment*, *115*, 2008–2024.

Iiames, J., Jr., Pilant, A., & Lewis, T. (2004). *In situ estimates of forest LAI for MODIS data validation Remote sensing and GIS accuracy assessment*. Boca Raton, FL: CRC Press.

Iiames, J. S., Congalton, R., Pilant, A., & Lewis, T. (2008). Validation of an integrated estimation of loblolly pine (*Pinus taeda* L.) leaf area index (LAI) using two indirect optical methods in the southeastern United States. *Southern Journal of Applied Forestry*, *32*, 101–110.

Kucharik, C. J., Norman, J. M., Murdock, L. M., & Gower, S. T. (1997). Characterizing canopy nonrandomness with a multiband vegetation imager (MVI). *Journal of Geophysical Research-Atmospheres*, *102*, 29455–29473.

Lacaze, R., Chen, J. M., Roujean, J. L., & Leblanc, S. G. (2002). Retrieval of vegetation clumping index using hotspot signatures measured by POLDER instrument. *Remote Sensing of Environment*, *79*, 84–95.

Law, B. E., Cescatti, A., & Baldocchi, D. D. (2001). Leaf area distribution and radiative transfer in open-canopy forests: Implications for mass and energy exchange. *Tree Physiology*, *21*, 777–787.

Law, B. E., Van Tuyl, S., Cescatti, A., & Baldocchi, D. D. (2001). Estimation of leaf area index in open-canopy ponderosa pine forests at different successional stages and management regimes in Oregon. *Agricultural and Forest Meteorology*, *108*, 1–14.

Leblanc, S. G., & Chen, J. M. (2001). A practical scheme for correcting multiple scattering effects on optical LAI measurements. *Agricultural and Forest Meteorology*, *110*, 125–139.

Leblanc, S. G., Chen, J. M., Fernandes, R., Deering, D. W., & Conley, A. (2005). Methodology comparison for canopy structure parameters extraction from digital hemispherical photography in boreal forests. *Agricultural and Forest Meteorology*, *129*, 187–207.

Leblanc, S. G., Chen, J. M., White, H. P., Cihlar, J., Roujean, J. L., & Lacaze, R. (2001). Mapping vegetation clumping index from directional satellite measurements. *Proceedings of the 8th International Symposium on Physical Signatures and Measurements in Remote Sensing, Aussois, France* (pp. 450–459). Toulouse, France.

Leblanc, S. G., Chen, J. M., White, H. P., Latifovic, R., Lacaze, R., & Roujean, J. L. (2005). Canada-wide foliage clumping index mapping from multiangular POLDER measurements. *Canadian Journal of Remote Sensing*, *31*, 364–376.

Lucht, W., Schaaf, C. B., & Strahler, A. H. (2000). An algorithm for the retrieval of albedo from space using semiempirical BRDF models. *IEEE Transactions on Geoscience and Remote Sensing*, *38*, 977–998.

Maignan, F., Breon, F. M., & Lacaze, R. (2004). Bidirectional reflectance of Earth targets: Evaluation of analytical models using a large set of spaceborne measurements with emphasis on the HotSpot. *Remote Sensing of Environment*, *90*, 210–220.

Miller, J. B. (1967). A formula for average foliage density. *Australian Journal of Botany*, *15*, 141.

Mo, X. G., Chen, J. M., Ju, W. M., & Black, T. A. (2008). Optimization of ecosystem model parameters through assimilating eddy covariance flux data with an ensemble Kalman filter. *Ecological Modelling*, *217*, 157–173.

Morisette, J. T., Privette, J. L., & Justice, C. O. (2002). A framework for the validation of MODIS land products. *Remote Sensing of Environment*, *83*, 77–96.

Nilson, T. (1971). A theoretical analysis of the frequency of gaps in plant stands. *Agricultural Meteorology*, *8*, 25–38.

Pisek, J., Chen, J. M., Alikas, K., & Deng, F. (2010). Impacts of including forest understory brightness and foliage clumping information from multiangular measurements on leaf area index mapping over North America. *Journal of Geophysical Research-Biogeosciences*, *115*.

Pisek, J., Chen, J. M., Lacaze, R., Sonnentag, O., & Alikas, K. (2010). Expanding global mapping of the foliage clumping index with multi-angular POLDER three measurements: Evaluation and topographic compensation. *ISPRS Journal of Photogrammetry and Remote Sensing*, *65*, 341–346.

Pisek, J., Chen, J. M., Miller, J. R., Freemantle, J. R., Peltoniemi, J. I., & Simic, A. (2010). Mapping forest background reflectance in a boreal region using multiangle compact airborne spectrographic imager data. *IEEE Transactions on Geoscience and Remote Sensing*, *48*, 499–510.

Pisek, J., Chen, J. M., & Nilson, T. (2011). Estimation of vegetation clumping index using MODIS BRDF data. *International Journal of Remote Sensing*, *32*, 2645–2657.

Pisek, J., Lang, M., Nilson, T., Korhonen, L., & Karu, H. (2011). Comparison of methods for measuring gap size distribution and canopy nonrandomness at Järvselja RAMI (RAdiation transfer Model Intercomparison) test sites. *Agricultural and Forest Meteorology*, *151*, 365–377.

Roman, M. O., Schaaf, C. B., Woodcock, C. E., Strahler, A. H., Yang, X. Y., Braswell, R. H., et al. (2009). The MODIS (Collection V005) BRDF/albedo product: Assessment of spatial representativeness over forested landscapes. *Remote Sensing of Environment*, *113*, 2476–2498.

Ross, J. K. (1981). The radiation regime and architecture of plant stands. Norwell, MA.

Roujean, J. -L., Leroy, M., & Deschamps, P. -Y. (1992). A bidirectional reflectance model of the earth's surface for the correction of remote sensing data. *Journal of Geophysical Research*, *97*, 20455–20468.

Ryu, Y., Nilson, T., Kobayashi, H., Sonnentag, O., Law, B. E., & Baldocchi, D. D. (2010). On the correct estimation of effective leaf area index: Does it reveal information on clumping effects? *Agricultural and Forest Meteorology*, *150*, 463–472.

Ryu, Y., Sonnentag, O., Nilson, T., Vargas, R., Kobayashi, H., Wenk, R., et al. (2010). How to quantify tree leaf area index in an open savanna ecosystem: A multi-instrument and multi-model approach. *Agricultural and Forest Meteorology*, *150*, 63–76.

Schaaf, C. B., Gao, F., Strahler, A. H., Lucht, W., Li, X. W., Tsang, T., et al. (2002). First operational BRDF, albedo nadir reflectance products from MODIS. *Remote Sensing of Environment*, *83*, 135–148.

Schaaf, C. B., Liu, J., Gao, F., & Strahler, A. H. (2011). Aqua and Terra MODIS albedo and reflectance anisotropy products. In B. Ramachandran, C. O. Justice, & M. J. Abrams (Eds.), *Land Remote Sensing and Global Environmental Change* (pp. 549–561). New York: Springer.

Simic, A., & Chen, J. M. (2008). Refining a hyperspectral and multiangle measurement concept for vegetation structure assessment. *Canadian Journal of Remote Sensing*, *34*, 174–191.

Simic, A., Chen, J. M., Freemantle, J. R., Miller, J. R., & Pisek, J. (2010). Improving clumping and LAI algorithms based on multiangle airborne imagery and ground measurements. *Geoscience and Remote Sensing, IEEE Transactions on*, *48*, 1742–1759.

Sonnentag, O., Chen, J. M., Roberts, D. A., Talbot, J., Halligan, K. Q., & Govind, A. (2007). Mapping tree and shrub leaf area indices in an ombrotrophic peatland through multiple endmember spectral unmixing. *Remote Sensing of Environment*, *109*, 342–360.

Sprintsin, M., Cohen, S., Maseyk, K., Rotenberg, E., Grunzweig, J., Karnieli, A., et al. (2011). Long term and seasonal courses of leaf area index in a semi-arid forest plantation. *Agricultural and Forest Meteorology*, *151*, 565–574.

Sprintsin, M., Karnieli, A., Berliner, P., Rotenberg, E., Yakir, D., & Cohen, S. (2007). The effect of spatial resolution on the accuracy of leaf area index estimation for a forest planted in the desert transition zone. *Remote Sensing of Environment*, *109*, 416–428.

Su, L., & Song, C. (2008). Derivation of leaf clumping index using BRDF models and MISR/MODIS data. *NASA Carbon Cycle and Ecosystems Program Joint Workshop, April 28–May 2. Adelphi, MD USA*.

Vermote, E. F., El Saleous, N. Z., & Justice, C. O. (2002). Atmospheric correction of MODIS data in the visible to middle infrared: First results. *Remote Sensing of Environment*, *83*, 97–111.

Walcroft, A. S., Brown, K. J., Schuster, W. S. F., Tissue, D. T., Turnbull, M. H., Griffin, K. L., et al. (2005). Radiative transfer and carbon assimilation in relation to canopy architecture, foliage area distribution and clumping in a mature temperate rainforest canopy in New Zealand. *Agricultural and Forest Meteorology*, *135*, 326–339.

Wang, Y. J., Lyapustin, A. I., Privette, J. L., Cook, R. B., SanthanaVannan, S. K., Vermote, E. F., et al. (2010). Assessment of biases in MODIS surface reflectance due to Lambertian approximation. *Remote Sensing of Environment*, *114*, 2791–2801.

Wanner, W., Li, X., & Strahler, A. H. (1995). On the derivation of kernels for kernel-driven models of bidirectional reflectance. *Journal of Geophysical Research*, *100*, 21077–21089.

Woodcock, C. E., & Strahler, A. H. (1987). The factor of scale in remote-sensing. *Remote Sensing of Environment*, *21*, 311–332.